Key Points:
- In the candidate Chang'E-5 landing region, rocks are mostly concentrated around rocky ejecta craters
- Crater SFD analysis indicates that the eastern part of the region is younger than the western part
- Joint analysis of rock abundance and crater density reveals relationships between them and between rock abundance and crater maturation

Rock Abundance and Crater Density in the Candidate Chang'E-5 Landing Region on the Moon

Bo Wu[1] , Jun Huang[2], Yuan Li[1], Yiran Wang[1], and Jin Peng[2]

[1]Department of Land Surveying and Geo-Informatics, The Hong Kong Polytechnic University, Hong Kong, [2]China Academy of Space Technology, Beijing, China

Abstract Chang'E-5 is China's first lunar sample-return mission, which will be launched in 2019. Understanding the distribution of rocks and craters in the candidate landing region is important for selecting suitable landing sites and studying the surface geology. This paper first separately investigates rock abundance and crater density in the candidate landing region, then provides a joint analysis of them, for the purposes of identifying potential hazards for safe landing and their geological implications. The results indicate that in the region, rocks are mostly concentrated around rocky ejecta craters. About 90% of the region has a rock abundance (the fractional area covered by rocks) of less than 1%. The average crater density is about 250 craters ($\geq$ 100 m in diameter) per 100 km^2; on average, 13.5% of the region is covered by craters. The surface ages of geologic units in the region estimated using crater size-frequency distribution indicate that the eastern part of the region is younger than the western part. The joint analysis of rock abundance and crater density identifies local areas that are relatively unfavorable for safe landing. The joint analysis also indicates an exponential relationship between overall rock abundance and crater density, and a roughly linear relationship between overall rock abundance and surface age. Furthermore, the joint analysis indicates an inverse correlation between rock abundance and the relative maturation of craters. The presented research and results will be helpful for identifying suitable landing sites for the Chang'E-5 lander. They also provide fresh insights into lunar surface geology.

Plain Language Summary Chang'E-5 is China's first lunar sample-return mission, which will be launched in 2019. Understanding the distribution of rocks and craters in the candidate landing region is important for selecting suitable landing sites and studying the surface geology. This paper first separately investigates rock and crater distributions in the candidate landing region, then provides a joint analysis of them, to identify potential hazards for safe landing and their geological implications. The results indicate that in the region, rocks are mostly concentrated around rocky ejecta craters. About 90% of the region are almost rock free. There are about 250 craters ($\geq$ 100 m in diameter) per 100 km^2. The surface ages of units in the region estimated from the crater distributions indicate that the eastern part of the region is younger than the western part. The joint analysis of rock and crater distributions identifies local areas that are relatively unfavorable for safe landing. The joint analysis also indicates relationships among the rock distribution, crater distribution, maturation of craters, and surface ages. The presented research and results will be helpful for identifying suitable landing sites for the Chang'E-5 lander. They also provide fresh insights into lunar surface geology.

1. Introduction

The Chang'E-5 mission, scheduled to be launched in 2019, is a sample-return mission that represents the third phase of the Chinese Lunar Exploration Program (Zou & Li, 2017), subsequent to previous missions from the first phase of orbiting (the Chang'E-1 and Chang'E-2; Ouyang et al., 2010) and the second phase of soft-landing (the Chang'E-3; C. Li et al., 2015). Chang'E-5 is scheduled to land in the northern Oceanus Procellarum and return with up to 2 kg of lunar regolith and drill core samples (Zou & Li, 2017). The candidate landing region of Chang'E-5 is near the Mons Rümker volcanic complex (Zeng et al., 2017) in the northern Oceanus Procellarum, which covers an area of 10° × 3° (53–63°W, 41–44°N), as shown in Figure 1.

Rocks are one of the major features of the lunar surface and can cause potential hazards for the lander and rover. Rock abundance, defined as the cumulative fractional area (CFA) covered by rocks with respect to the rock diameter (normally for rocks ≥10 cm in diameter; Golombek & Rapp, 1997), is a critical factor when selecting a suitable landing site for any landing mission (Rosa et al., 2012; Wu et al., 2014). Rock
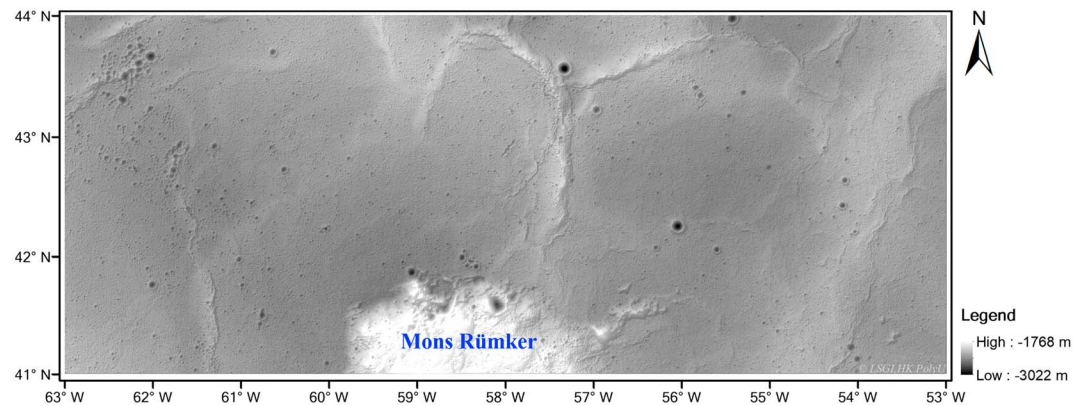
Figure 1. The candidate landing region of Chang'E-5 (53–63°W, 41–44°N). The background map is the shaded SLDEM2015 (Barker et al., 2016) with a resolution of 512 pixels per degree.

abundance on the Martian surface has been extensively investigated due to the successful Mars landing missions in the past decades. For example, thermal emission data from the Viking Infrared Thermal Mapper (Christensen, 1986) and the Mars Global Surveyor Thermal Emission Spectrometer (Nowicki & Christensen, 2007) were used to develop rock abundance models based on temperature contrasts between rocks and fine components. These studies benefited from the large coverage of the orbital data and provided important clues for selecting landing sites for the Mars Pathfinder (Golombek & Rapp, 1997) and other Mars missions. However, the resolution of the data was very low (e.g., 1 pixel per degree for the Viking Infrared Thermal Mapper data). Researchers have also used ground images obtained by cameras onboard landers or rovers to analyze size-frequency distribution (SFD) of rocks and rock abundance since the two successful Viking missions (Moore & Keller, 1991). Golombek and Rapp (1997) developed an exponential function of the rock abundance model based on rock measurements at the two Viking landing sites, which yields the CFA covered by rocks versus diameter on the basis of fracture and fragmentation theory (Golombek & Rapp, 1997; Moore et al., 1987; Moore & Keller, 1991). This exponential model has been widely used to represent rock abundance on the Martian surface, as it generally matched the rock SFD curves from real measurements taken from ground images at various landing sites, including the Mars Pathfinder (Golombek & Rapp, 1997), Mars Exploration Rover (Golombek et al., 2003), and Mars Science Laboratory (Golombek et al., 2012). For upcoming Mars landing missions, for example, the ExoMars mission, one criterion for selecting a landing site is that the rock abundance is less than 7% (Pajola et al., 2017); for the InSight mission, it should be less than 10% (Golombek et al., 2017). However, there has been less research concerning rock abundance on the lunar surface, due to the lack of landing missions since the late 1970s. Shoemaker et al. (1968) studied the SFDs of rocks using the Surveyor I and III photographs. Cintala and McBride (1995) investigated the rock distributions using the Surveyor I, III, VI, and VII photographs and the Lunar Orbiter photographs. They used the power law function to fit the SFDs of rocks. Bandfield et al. (2011) analyzed the rock concentration on the lunar surface on an almost global scale using measurements from the Lunar Reconnaissance Orbiter (LRO) Diviner radiometer. Rosa et al. (2012) used LRO narrow-angle camera (NAC) images with resolutions between 0.6 and 1.0 m per pixel, and visually identified hundreds of rocks in the vicinity of the chosen landing sites of the European Space Agency's Lunar Lander mission. More recently, Di et al. (2016) identified hundreds of rocks from ground images taken by the Chang'E-3 rover and suggested exponential curves for rock SFD. Basilevsky et al. (2015) also investigated the rock measurements from the Chang'E-3 rover and compared the results with those from the Lunokhod 1 as both of them explored the northwestern part of Mare Imbrium. Watkins, Jolliff, et al. (2018) and Watkins, Mistick, et al. (2018) used the power law function to fit the relationship between the cumulative number of boulders and the boulder diameters around several lunar impact craters. Y. Li and Wu (2018) studied the SFDs of rocks in several regions (the Chang'E-3, Luna 17, and Luna 23 landing sites) on the lunar surface using high-resolution orbital and decent images and proposed a rock abundance model with an exponential form, which was used in this research. Noted that the power law function was not considered in this research. The power law

function is suitable for fitting the distributions of relatively larger rocks (e.g., boulders >25 cm in diameter); however, it may overestimate the number of rocks at smaller diameters (Golombek & Rapp, 1997). Also, an exponential form of the rock abundance model can be better explained by the fracture and fragmentation theory (Gilvarry, 1961; Golombek & Rapp, 1997).

Craters are another type of distinct geological feature on the lunar surface. Craters are regarded as hazardous features in landing site assessment, due to the morphological characteristics of the internal slopes and protuberant crater rims. The spatial distribution and density of craters are critical factors in landing site selection (Brady et al., 2009; Golombek et al., 2017; Huertas et al., 2006; Serrano & Seraji, 2007). In addition, the SFD of craters provides useful information for inferring surface ages. In earlier studies, the relationship between the crater SFD at the Apollo landing sites and the radiometric ages of the returned rock samples was established for the determination of crater chronology (Hartmann, 1964; Shoemaker et al., 1970). Furthermore, Neukum (1983) and Neukum et al. (2001) developed crater production functions for estimating surface ages based on the SFD of craters, which has been widely used in the past.

Previous researchers also studied the distributions of rocks and craters to better understand other geologic characteristics of the lunar surface (Bart & Melosh, 2010a; Mendell, 1976; Xiao & Strom, 2012). Xiao and Strom (2012) pointed out that a thinner regolith, which is more easily penetrated to reach bedrock during impact cratering, is likelier to result in a rockier surface. Bart and Melosh (2010a) studied the relationship between rock ejection velocity during impact cratering, and Bart and Melosh (2010b) further investigated the distribution of boulders ejected from craters. Krishna and Kumar (2016) investigated the shape and size of ejecta boulders as well as secondary craters distributed around the Censorinus crater on lunar surface. Previous studies have noted an inverse correlation between rock abundance and crater age (Basilevsky et al., 2013; Ghent et al., 2014), as most of the rocks are crater ejects due to impact events and will be degraded over time by space weathering and micrometeorite impacts (Mendell, 1976). Therefore, younger craters are more likely to have elevated rock abundance values. Charalambous (2014) and Golombek et al. (2017) suggested that the relationship between rock abundance and crater maturity can be represented by a Negative Binomial (NB) model (Charalambous, 2014).

This paper presents a systematic study of rock abundance and crater density in the candidate Chang'E-5 landing region, for the purposes of identifying potential hazards for safe landing and evaluating their geological implications. The second section describes the rock abundance inside the region. The third section presents the crater densities inside the region and the surface ages of the geologic units in the region, as estimated from the crater SFD. The fourth section presents joint analyses of rock abundance and crater density in the region, and finally, a concluding section summarizes what has been learned from this research.

2. Rock Abundance in the Candidate Chang'E-5 Landing Region

2.1. Rock Detection Using an LRO NAC Image Mosaic

LRO NAC imagery features the highest spatial resolution (0.5–2 m per pixel) of lunar surface images currently available from orbital observation (Robinson et al., 2010). There are hundreds of LRO NAC images of the candidate landing region available, and most have a resolution of 1.5 m per pixel. These images were downloaded from NASA's Planetary Data System and used to generate an image mosaic with a resolution of 1.5 m per pixel for rock detection. The LRO NAC image mosaic was generated using image-processing software based on the Integrated System for Imagers and Spectrometers (ISIS) provided by the United States Geological Survey. First, the images were batch-processed by ISIS to reach their Level 2 products, which are ortho-rectified images based on a digital elevation model (DEM) derived from the LRO Lunar Orbiter Laser Altimeter data. Second, tie points were automatically detected between any two neighboring images, and on this basis an affine transformation model was used to adjust the locations of the images to remove geometric discrepancies between the images. Third, histogram matching among the images was carried out to improve their radiometric consistency. Finally, the processed individual images were merged to generate a mosaic covering the entire landing region, as shown as the background image in Figure 2a. The image mosaic is in the geographic coordinate system (GCS Moon 2000) using the Mercator projection system.
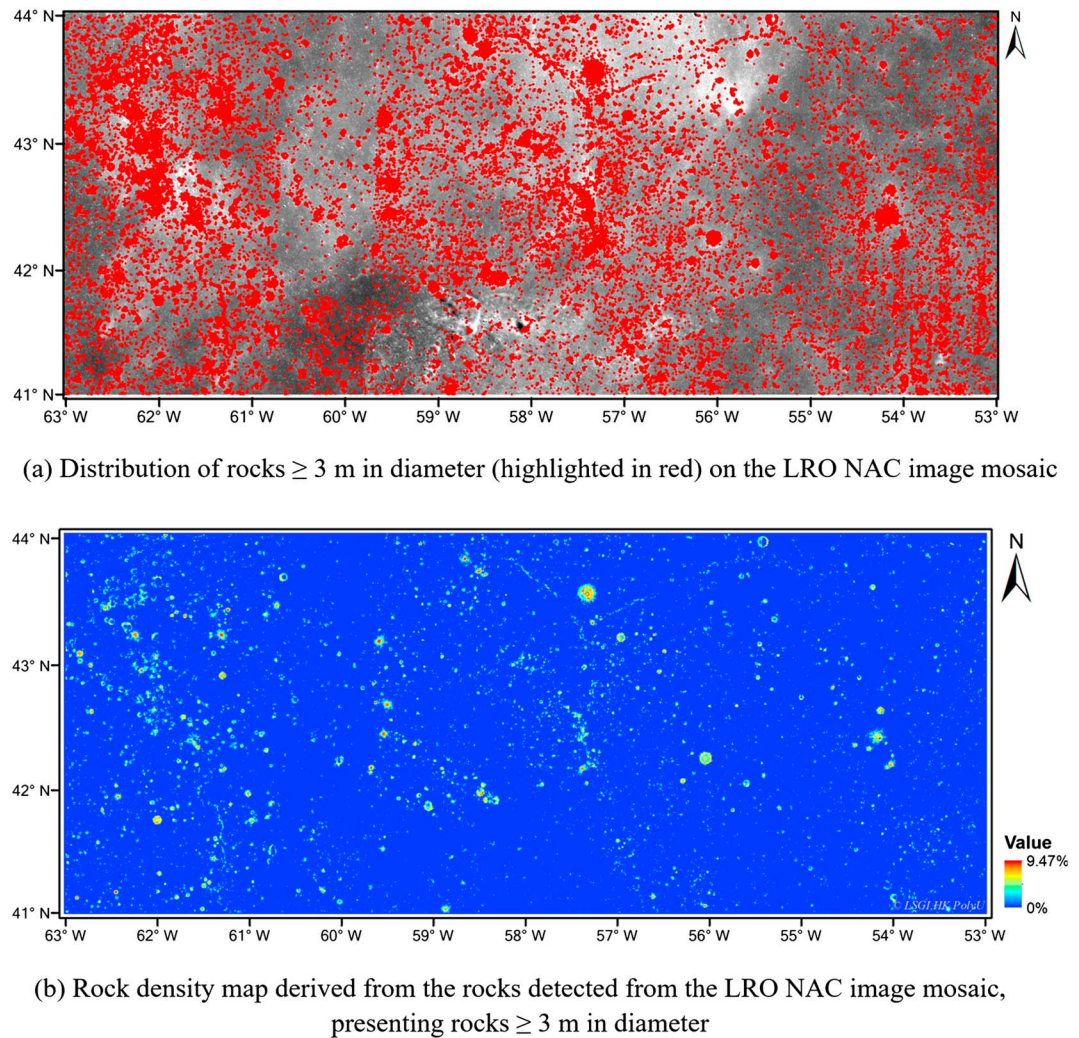
(a) Distribution of rocks ≥ 3 m in diameter (highlighted in red) on the LRO NAC image mosaic

(b) Rock density map derived from the rocks detected from the LRO NAC image mosaic, presenting rocks ≥ 3 m in diameter

Figure 2. Detected rocks and rock density map in the candidate Chang'E-5 landing region. LRO = Lunar Reconnaissance Orbiter; NAC = narrow-angle camera.

An automatic rock detection algorithm developed by Y. Li and Wu (2018) was used to extract rocks from the LRO NAC image mosaic. The fundamental idea of this algorithm is that the brightness distributions of ground features present in the image differ due to their different relief properties. Generally, rocks and the sunward side of craters correspond to bright pixels on the image, but their shadows are cast in opposite directions. Rocks can thus be identified by comparing gradient differences along the illumination direction. Finally, the algorithm fits the clusters of rock pixels into ellipses representing the boundaries of rocks. Details of this rock detection algorithm can be found in our previous work (Y. Li & Wu, 2018).

An application of this algorithm to the LRO NAC image mosaic identified over 510,000 rocks in the candidate landing region. The detected rocks have a minimum size of 3 m (two pixels on the image). To ensure the reliability of the detected rocks, a manual checking process was further performed by two independent operators, with the assistance of a grid with a cell size of 3 m × 3 m overlaid on the image mosaic. The final distribution of detected rocks is shown in Figure 2a. Their size ranges from 3 to 44.6 m. A rock density map presenting the fractional area covered by rocks in each 250-m × 250-m tile (a size with statistical significance and also meaningful for comparison with LRO Diviner Radiometer data) is presented in Figure 2b. The maximum areal fraction of rocks (≥ 3 m in diameter) in the candidate landing region is 9.47%.

2.2. Rock Abundance in the Candidate Landing Region

As rocks may cause potential hazards to the lander and rover, it is important to examine the rock abundances in the candidate landing region. The rock density map in Figure 2b only reflects the distribution of rocks with sizes larger than 3 m within the candidate landing region, due to the limitation of the image resolution. However, analysis of rock distribution for landing site assessment or surface geology requires understanding the overall distribution of rocks of the full size range. One possible way to infer the overall distribution of all rocks from a definite number of rocks with sizes above a particular value is to refer to a rock abundance model, for example, the one proposed by Y. Li and Wu (2018). Following fracture and fragment theory (Gilvarry, 1961), Y. Li and Wu (2018) proposed a rock abundance model for the lunar surface based on the SFDs of rocks detected from multiple-source high-resolution images covering different regions on the Moon, including the Chang'E-3 descent images (0.02–0.17 m per pixel) and LRO NAC images (1.1 m per pixel) covering the Chang'E-3 landing site, LRO NAC images (0.3–0.35 m per pixel) covering the Luna 17 and 23 landing sites, and LRO NAC image mosaics (1.5 m/pixel) covering other regions. The rock abundance model has the following format (Y. Li & Wu, 2018):

$$F_k(D) = ke^{-(0.5648+0.01285/k)D} \tag{1}$$

where k is the rock abundance and $F_k(D)$ refers to the areal fraction of rocks larger than D in diameter. This rock abundance model describes the overall CFA of rocks versus their diameters.
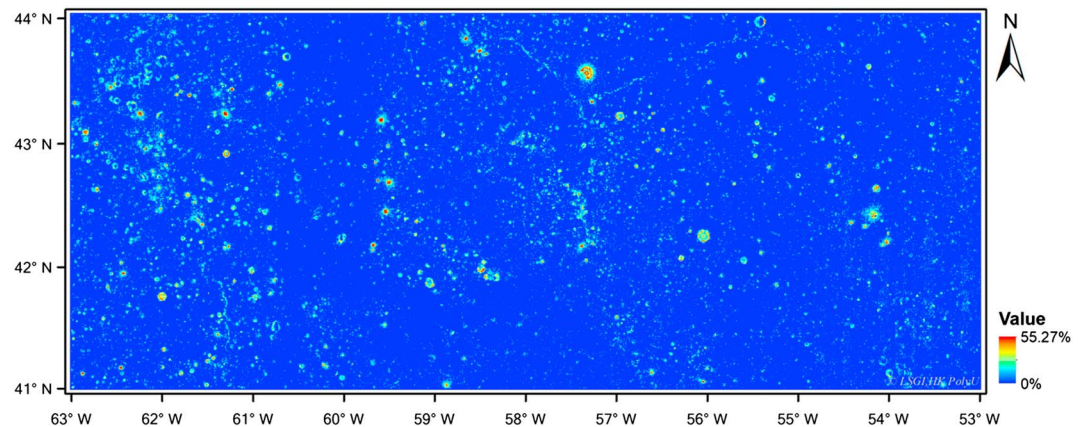
Based on this rock abundance model, the rock abundances for each 250-m × 250-m tile of the candidate landing region can be derived by extrapolating from the extracted rocks (≥ 3 m in diameter) to rocks of all possible sizes in the tile, from which a rock abundance map can be generated, as shown in Figure 3a. Based on the rock abundance map and referring to Figure 1, it can be seen that rocks are mostly concentrated around rocky ejecta craters and some are along the wrinkle ridges. The smooth terrain away from craters is generally rock free. The highest rock abundance in the candidate landing region is 55.27%, as shown in Figure 3b, with clusters of large rocks located at the center of a crater (59.6769°W, 42.1785°N).

## 2.3. Comparison With LRO Diviner Radiometer Data

Bandfield et al. (2011) proposed a method using LRO Diviner radiometer data to measure rock concentration on the lunar surface, based on the contrasting thermal conductivities between rocks and lunar regolith. The latest rock concentration map on lunar surface (covering all longitudes and 80°S to 85°N) generated using this method was released on the Planetary Data System Geosciences Node (http://ode.rsl.wustl.edu/moon/index.aspx); in this section, we compare this map with our rock abundance map in the candidate landing region.

The Diviner rock concentration map has a resolution of 128 pixels per degree (about 250 m at the equator) and each pixel presents the areal fraction of rocks larger than ~ 1.0 m in diameter (Bandfield et al., 2011). To compare our results with the Diviner rock concentration map, we binned the rocks detected in the candidate landing region into pixels covering the same region of each Diviner bin, and recalculated the areal fraction of rocks ≥1.0 m based on the rock abundance model (equation (1)). The differences between our results and the Diviner rock concentration map are shown in Figure 4. Figure 4a shows the overall differences between the rock abundances derived from our results and the Diviner results (ours minus the Diviner results) in the candidate landing region. In general, our results are consistent with the Diviner map, with an average absolute difference of 0.45%. But in some places the differences between the two datasets can be as large as 23%. Figure 4b shows detailed examples of these extreme cases.

The upper row in Figure 4b shows an extreme case of our result being greater than the Diviner result. The fractional area of rocks (≥ 1.0 m in diameter) derived from our result has a high value of 27.7%, while the Diviner result is only 5.9%, presenting a positive difference of 21.8%. It is clear in this case that our higher rock abundance is more reasonable than the Diviner result. The reason for this discrepancy might be that because the rock abundance derived from Diviner data is based on Planck's radiance law, small terrain features (such as small craters) with various slopes within the field of view of the Diviner measurements may have a range of temperatures and lead to erroneous results at some level (Bandfield et al., 2011). This may also relate to the much higher spatial resolution of the LRO NAC images used for rock detection in our analysis, compared with

(a) Rock abundance map derived based on the rocks detected from the LRO NAC image mosaic and the rock abundance model (Li and Wu, 2018)
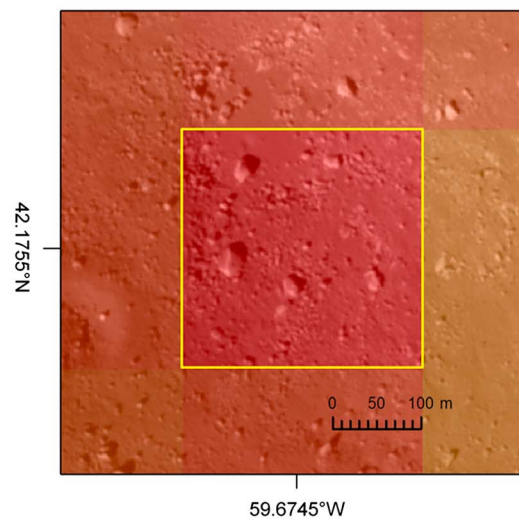
(b) The tile (yellow rectangle) with the highest rock abundance value of 55.27% shown on the LRO NAC image
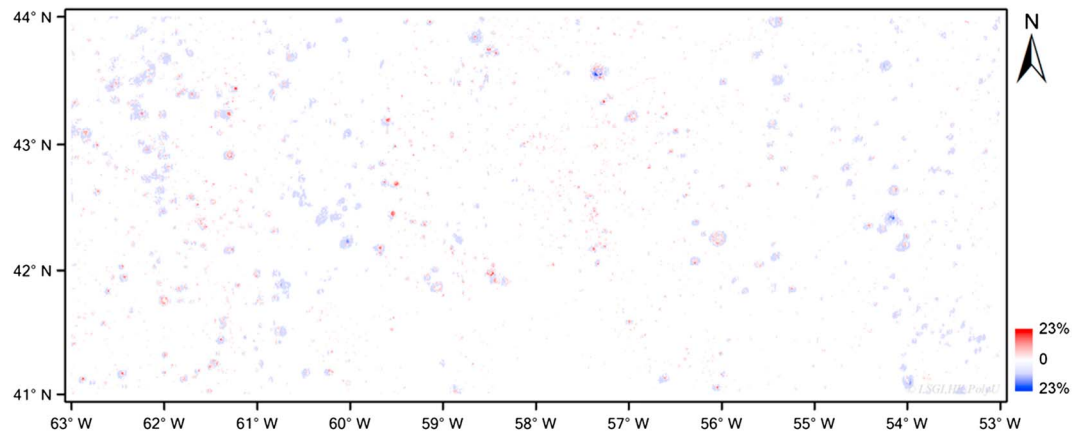
Figure 3. Rock abundance map of the candidate landing region; each pixel presents the overall rock abundance of a surface tile of 250 m × 250 m. LRO = Lunar Reconnaissance Orbiter; NAC = narrow-angle camera.

the resolution of the Diviner data. The bottom row in Figure 4b shows the other extreme case of our result being less than the Diviner result. This discrepancy is related to the illumination conditions of the images used for rock detection. Unfavorable illumination conditions such as a large sunlight incidence angle, which causes dark shadows in craters, will lead to the failure of rock detection and result in our rock abundance measurements being less than the Diviner results. Fortunately, such areas only cover about 1% of the total area of the candidate landing region.

3. Crater Density in the Candidate Chang'E-5 Landing Region

3.1. Crater Detection in the LRO NAC Image Mosaic

Craters are also potential hazards to the lander and rover, and investigation on the crater distribution is important in landing site assessment. In addition, the crater SFD is also important for crater chronology.

(a) Difference map between the rock abundances in the candidate landing region. Red pixels denote areas where our values are greater than the Diviner values, and blue pixels denote areas where our values are less
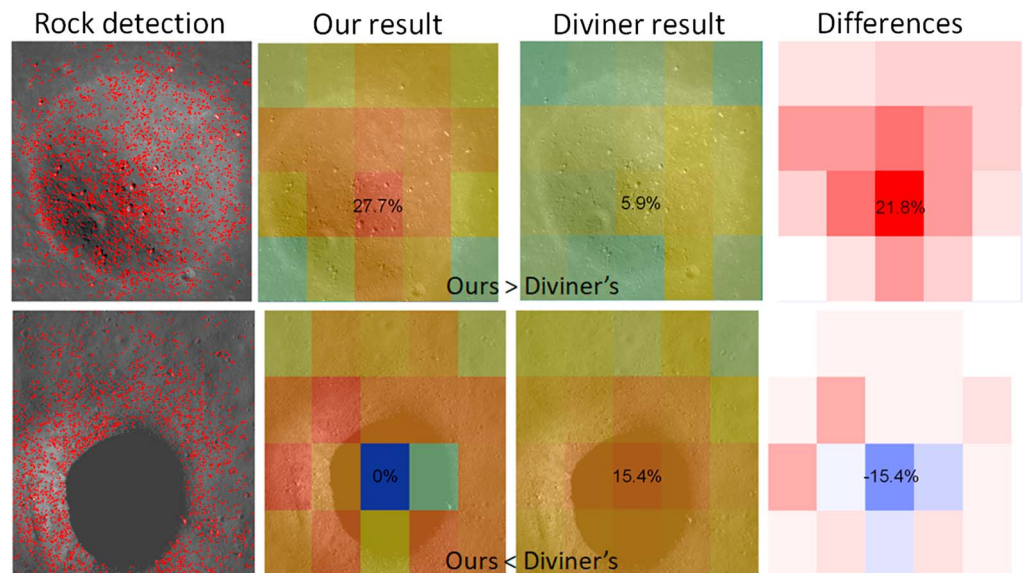
(b) Enlarged views providing a detailed comparison between our results and the Diviner results

Figure 4. Differences between the rock abundances derived from our results and the Diviner results (ours minus the Diviner results).

We developed an active machine learning approach (Wang et al., 2018) and used it for automatic crater detection on the LRO NAC image mosaic in this study. This approach involves two processes: training and detection. The training process begins with a classifier trained by dozens of positive samples (craters) and negative samples (non-craters). This classifier is applied to the image to generate an initial set of crater detection results. Next the approach actively asks for annotations for the detection results, with extra 3-D information derived from the corresponding DEM. Based on this feedback, the detected results are classified into correct detections and wrong detections, and they are then added to the positive and negative training samples, respectively. Thus, the training pool can be updated and enriched, allowing the classifier to be retrained to achieve better performance. After several iterations, the trained
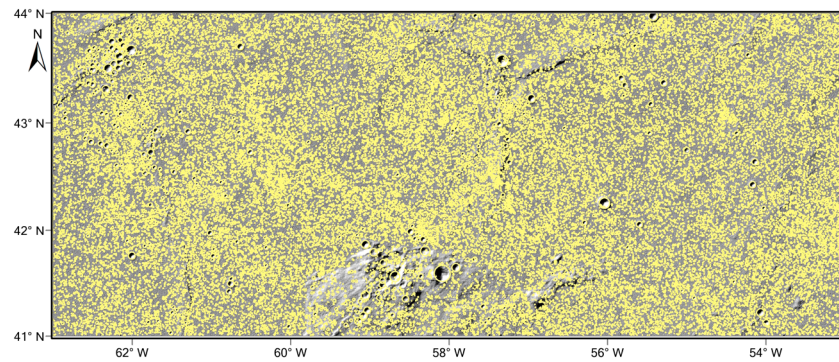
Figure 5. Distribution of craters (≥ 100 m in diameter) detected on the Lunar Reconnaissance Orbiter narrow-angle camera image mosaic in the candidate landing region.

classifier can be used for automatic crater detection on the entire LRO NAC image mosaic in the candidate landing region.

In this study, we aim to extract all craters ≥100 m in diameter. Although the automatic crater detection approach can detect craters with smaller sizes, its detection rate will decrease for craters with smaller sizes. Therefore, craters less than 100 m in size are ignored in this study. Furthermore, to ensure the reliability of the detected craters, a manual checking process was further performed by two independent operators with the assistance of a grid with a cell size of 100 m × 100 m overlaid on the image mosaic, to remove artifacts and digitize missing craters. Ultimately, over 48,200 craters were detected in the candidate landing region. The minimum size of the craters was 100 m and the maximum size was 4.5 km. Figure 5 shows the distribution of the detected craters.

3.2. Crater Density in the Candidate Landing Region

To better understand the distribution of craters in the candidate landing region, crater density maps in terms of numbers and area were generated, as shown in Figure 6. Crater density in terms of numbers was determined by calculating the number of craters in a moving circular window of 100 km^2, while crater density in terms of area is defined by the percentage of each 100-km^2 area covered by craters.

Crater density in terms of numbers as shown in Figure 6a reveals the concentration of crater distribution. Larger density represents a more serious situation involving clusters of relatively small craters. In the candidate landing region, the average density in terms of numbers is about 250 craters (≥ 100 m in diameter) per 100-km^2 area, and the maximum is 550, which is located in the middle west part (~42.5°N, 60°W) of the region. The local regions close to the foot of Mons Rümker and the wrinkle ridges in the middle and east parts of the region have relatively large densities in terms of numbers. The crater density in terms of area as shown in Figure 6b can be generally considered to represent the possibility of a lander landing in a crater. In the candidate landing region, the average density in terms of area is about 13.5% in a unit area of 100 km^2, and the maximum is 40%, which is located in the northwest corner of the region, where there is a cluster of relatively big craters.

3.3. Crater SFD for Surface Age Estimation

The SFD of craters (Hiesinger et al., 2003; Neukum, 1983; Neukum et al., 2001) was analyzed to estimate the surface ages of the geologic units in the candidate landing region. Qian et al. (2018) investigated the surface ages of different geologic units around the Mons Rümker area, in which the boundaries of geologic units were determined based on a false color composite map derived from the Kaguya Multiband Imager (MI) data and titanium and iron variations. In this study we followed the same strategy and identified eight geologic units inside the candidate landing region, which include five mare units (Im1, Im2, Em1, Em3, and Em4) and three Rümker plateau units (IR1, IR2, and IR3), as shown in Figure 7a. The names of the units are identical with those in Qian et al. (2018) for purpose of comparison.
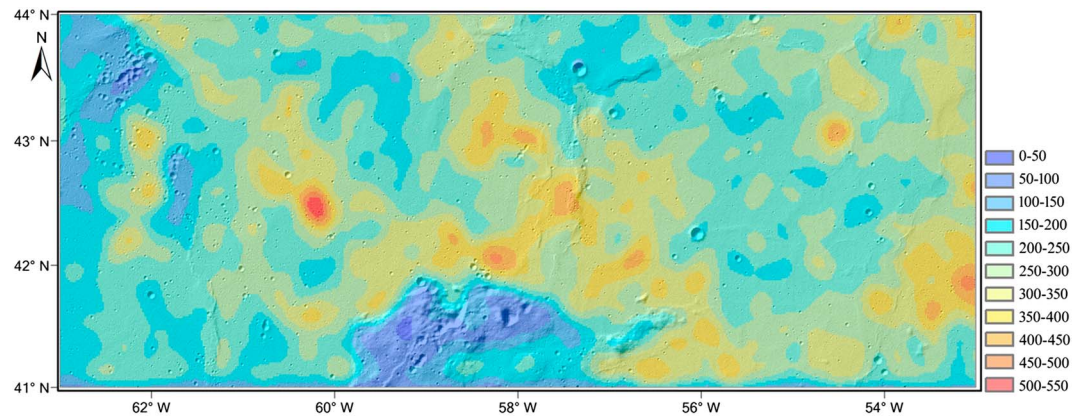
(a) Crater density in terms of numbers measured from the LRO NAC image mosaic
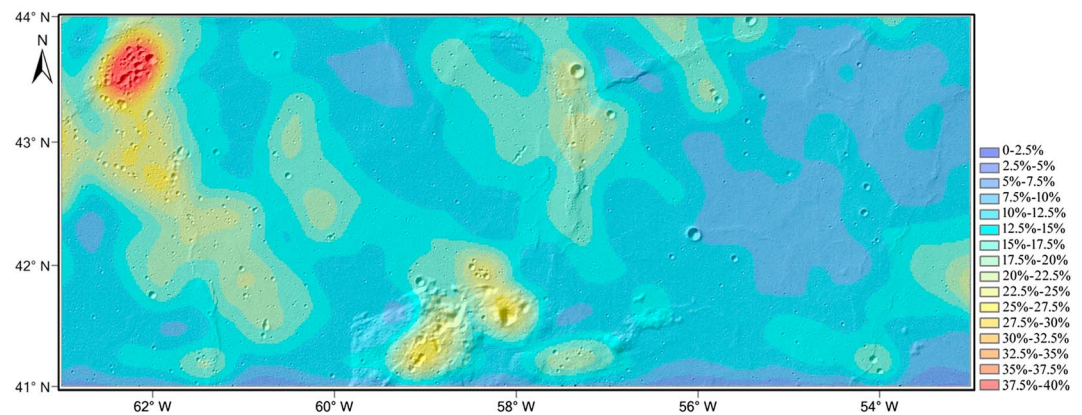
(b) Crater density in terms of area measured from the LRO NAC image mosaic

Figure 6. Crater density of the region calculated in a moving circular window of 100 km^2. LRO = Lunar Reconnaissance Orbiter; NAC = narrow-angle camera.

To estimate the surface ages of the units, we used SFD analysis based on the crater production function proposed by Neukum et al. (2001) and the CraterStats software suite. In cratering chronology, secondary craters add ambiguities in age estimation, and therefore, they must be excluded before dating the surface age. The secondary craters in the candidate landing region are basically caused by ejecta from three primary craters: Copernicus, Harpalus, and Pythagoras (Qian et al., 2018; Scott & Eggleton, 1973). To minimize the influence of secondary craters, only relatively large craters (≥500 m in diameter) were used for the SFD analysis, and for craters larger than 500 m, a manual checking process was further carried out to remove possible secondary craters based on clues such as clustering distribution and visual distinctness from primary craters (Guo et al., 2018; Robbins & Hynek, 2014; Wilhelms et al., 1987). The estimated surface ages of the geologic units in the candidate landing region are shown in Figure 7a, and the cumulative crater size-frequency plots for each unit are shown in Figure 7b.

The Rümker plateau units (IR1, IR2, and IR3) are the three oldest units in this region. The western mare units (Im1 and Im2) are Imbrian aged (~3.4–3.5 Ga), representing the major stage of lunar mare eruptive volcanism, while the mare units surrounding Mons Rümker (Em1 and Em3) and the one in the east part of the region (Em4) are among the youngest mare basalts on the Moon. Our results are in general consistent with those of Qian et al. (2018). However, our age estimates for the two western mare units (Im1 and Im2) and two eastern mare units (Em3 and Em4) are older than those of Qian et al. (2018). A detailed comparison is shown in Table 1. Table 1 also lists the ages of three units (Im1, Im2, and Em4) with relatively large coverages estimated by Hiesinger et al. (2003), of which our results are
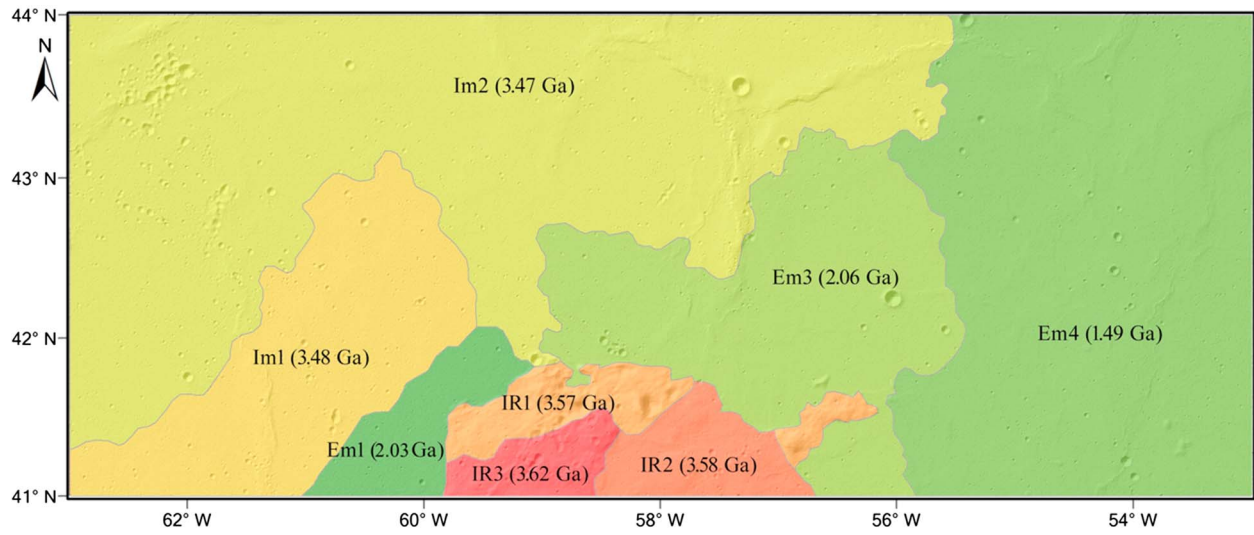
(a) The geologic units and estimated ages using the production function (Neukum et al., 2001)
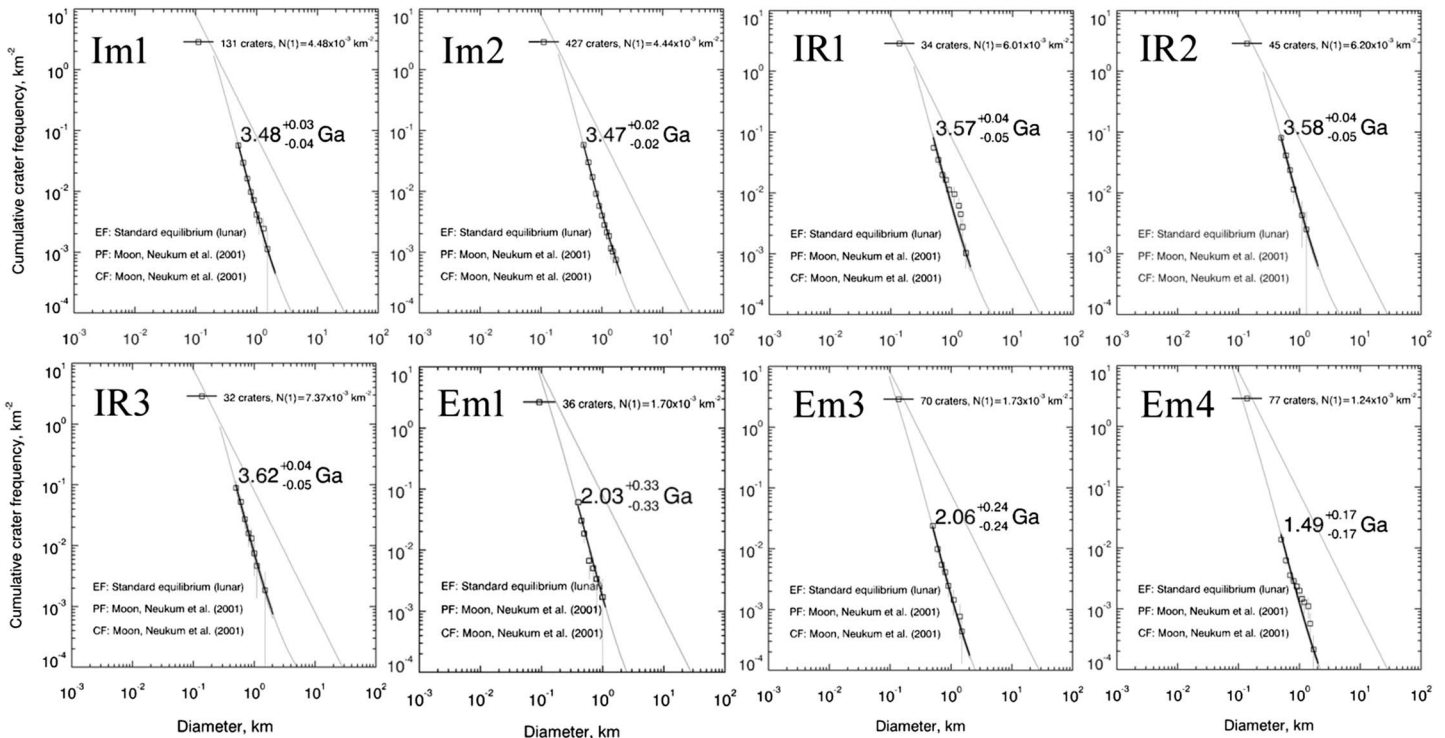
(b) Cumulative crater size-frequency plots for each unit

Figure 7. The estimated surface ages of the geologic units in the candidate landing region.

more consistent with those of Hiesinger et al. (2003) for Im1 and Im2. For Em4, our age estimate is the oldest and Qian et al.'s (2018) is the youngest, with Hiesinger et al.'s (2003) in the middle. The inconsistencies between our results and those of Hiesinger et al. (2003) and Qian et al. (2018) may relate to the different studying areas and different size ranges of craters for age estimation. Nevertheless, the overall consistency among the three results confirms the reliability of the estimated ages of the geologic units inside the landing region.

Table 1
Estimated Ages of Geological Units and Comparisons With the Results of Qian et al. (2018) and Hiesinger et al. (2003)

Unit	Estimated age (Ga; ours)	Calculated area (km^2; ours)	Estimated age (Ga; Qian et al., 2018)	Calculated area (km^2; Qian et al., 2018)	Estimated age (Ga; Hiesinger et al., 2003)
Im1	3.48(+0.03/−0.04)	2,315	3.42(+0.02/−0.02)	13,749	3.47
Im2	3.47(+0.02/−0.02)	7,378	3.39(+0.02/−0.02)	44,327	3.44
IR1	3.57(+0.04/−0.05)	585	3.71(+0.04/−0.05)	2,912	/
IR2	3.58(+0.04/−0.05)	561.53	3.58(+0.03/−0.04)	727	/
IR3	3.62(+0.02/−0.02)	354.6	3.51(+0.04/−0.06)	747	/
Em1	2.03(+0.33/−0.33)	596	2.3(+0.10/−0.10)	3,928	/
Em3	2.06(+0.24/−0.24)	2,961	1.51(+0.07/−0.07)	5,396	/
Em4	1.49(+0.17/−0.17)	5,607	1.21(+0.03/−0.03)	35,905	1.33

4. Joint Analysis of Rock Abundance and Crater Density

4.1. Joint Analysis of Rock Abundance and Crater Density for Safe Landing Consideration

Rock abundance and crater density are important engineering considerations when selecting suitable landing sites for robotic landing missions, so as to avoid hazards during touchdown and ensure better maneuverability of robotic vehicles (Rosa et al., 2012; Wu et al., 2014). For instance, one criterion for selecting the landing site for the ExoMars mission is that the rock abundance be less than 7% (Pajola et al., 2017). Crater rims and internal slopes can be hazardous for landing too (Brady et al., 2009; Huertas et al., 2006). Therefore, this study presents a joint analysis of rock abundance and crater density to identify local areas inside the candidate landing region that are unfavorable for safe landing.

First, the rock abundances inside the regions were classified into three categories: < 1%, 1–7%, and > 7%, using the two thresholds 1% and 7%. The Chang'E-3 landing site has a rock abundance of about 1% (Y. Li & Wu, 2018) and therefore is used here as a reference. 7% is considered the upper ceiling of rock abundance for a favorable landing site, based on the suggestions from other missions (Pajola et al., 2017) considering the rover traverse performance and the probability of encountering a rock hazard during landing. The classified rock abundance map is shown in Figure 8a. Statistically, about 90% (blue areas) of the candidate landing region has a rock abundance of less than 1%, and most such areas are flat terrain away from craters or ridges. About 9.1% (green areas) has a rock abundance between 1% and 7%, mainly around the outer rings of craters or along the slopes of ridges or lava flows. The remaining 0.9% (red areas) of the region has a rock abundance greater than 7%; these areas are mainly concentrated in and around large craters.

Second, the crater density map in terms of numbers was used for hazard evaluation, as it reveals the concentration of relatively small craters, which are potential hazards for safe landing. There is no specific criterion in previous studies for crater density in landing site assessment; therefore, this study uses the mean crater numbers (250 craters per 100 km^2) in the region and the value of the mean minus the standard deviation, which is 181 craters per 100 km^2, as two thresholds for classification. The classified crater density map is shown in Figure 8b. About 14% (blue areas) of the region has a crater density of less than 181 craters per 100 km^2. About 38.4% (green areas) has a crater density between 181 and 250 craters per 100 km^2. The remaining 47.6% (red areas) of the region has a crater density greater than 250 craters per 100 km^2. In this study, we treat these red areas with crater density greater than the mean value as relatively unfavorable for landing site selection.

Third, combining the criterion of rock abundance >7% and crater density greater than the mean value, an overlay analysis between the classified rock abundance map (generated based on the rock detection results from the LRO NAC image mosaic and the rock abundance model proposed by Y. Li and Wu (2018), as shown in Figure 8a) and the classified crater density map (generated based on the crater detection results from the LRO NAC image mosaic, as shown in Figure 8b) was carried out to generate a hazard map of the candidate landing region, as shown in Figure 8c. It shows the distribution of local areas with relatively high rock abundance (yellow) or high crater density (red). These local areas are considered to be relatively unfavorable for safe landing. It should be noted that surface slopes are also potential hazards for safe landing. The candidate landing region is covered by widespread mare basalts, and is generally flat except for Mons Rümker in the
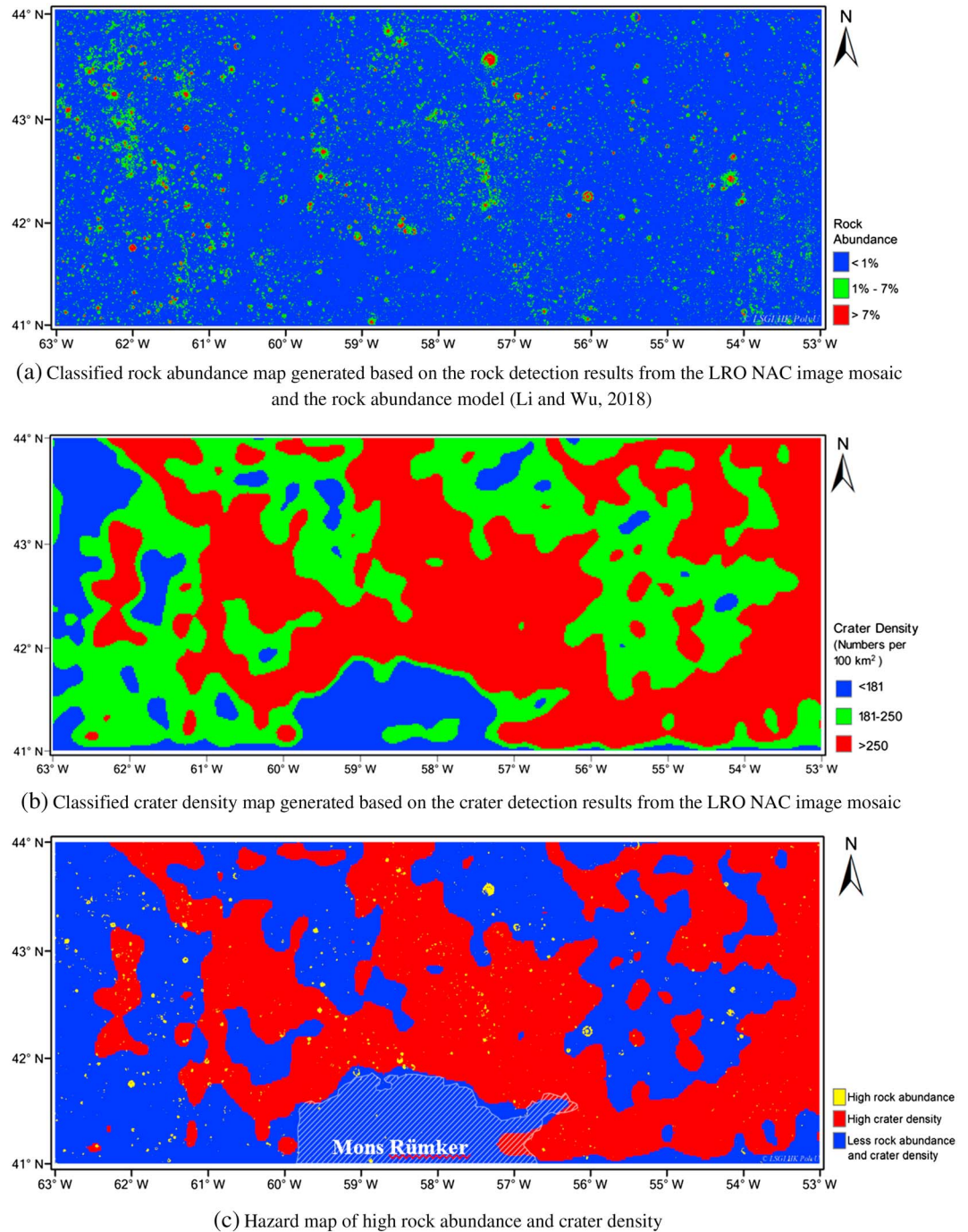
(a) Classified rock abundance map generated based on the rock detection results from the LRO NAC image mosaic and the rock abundance model (Li and Wu, 2018)

(b) Classified crater density map generated based on the crater detection results from the LRO NAC image mosaic

(c) Hazard map of high rock abundance and crater density

Figure 8. Joint analysis of rock abundance and crater density for safe landing considerations. LRO = Lunar Reconnaissance Orbiter; NAC = narrow-angle camera.

middle bottom part of the region. Slope analysis based on the DEM (shown in Figure 1) indicates that the mean slope of the area is 2.7° (at a baseline length of 120 m), with only 1% of the region exceeding a slope of 10°, which mainly occurs on the internal slopes of young craters and on the slopes of Mons Rümker. Similar findings about slopes in the region were also obtained by Quan et al. (2018). Therefore, surface slopes are ignored in this study.
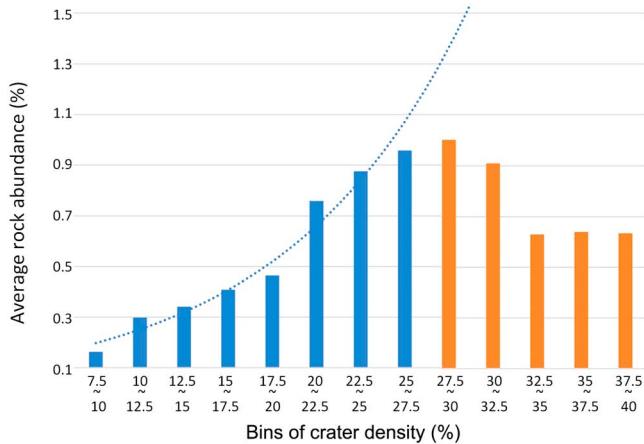
Figure 9. Correlation between crater density and rock abundance both derived from the LRO NAC image mosaic. The horizontal axis presents the crater density in terms of areas (refer to Figure 6b) binned into different classes and the vertical axis presents the corresponding average rock abundances in these bins. The blue dotted line is an exponential curve defined by equation (2).

4.2. Relationship Between Rock Abundance and Crater Density

From the rock abundance map shown in Figure 3a, it can be seen that rocks are mostly concentrated around rocky ejecta craters. Intuitively, there might be some relationship between crater density and rock abundance on the lunar surface. Crater density in terms of area is more suitable for this analysis, as large craters are likely to produce higher rock abundance. Crater densities inside the candidate landing region were binned into different classes, and the average rock abundance in each class was calculated; their relationships are illustrated in Figure 9. In Figure 9, crater densities less than 7.5% are ignored, as they cover very small areas in total across the region. From Figure 9, it can be seen that for classes with crater density $\leq 27.5\%$, higher rock abundance is related to higher crater density, which is consistent with our intuitive observation. This relationship can be approximately modeled by the following exponential function:

$$\widetilde{k} = 0.0009184e^{9.247d} \qquad (2)$$

where d is the mean crater density of a class and $\widetilde{k}$ is the corresponding mean rock abundance.

However, this exponential function only fits for classes with crater densities $\leq 27.5\%$ (the blue bars in Figure 9); for classes with crater densities $>27.5\%$ (the brown bars in Figure 9) the exponential curve deviates from the rock abundances derived based on the rock detection results from the LRO NAC image mosaic and the rock abundance model (Y. Li & Wu, 2018). One possible reason is that for local areas with large crater densities (i.e., $> 27.5\%$), rock detection results suffer from the appearance of large shadows (refer to the example in Figure 4b), which lead to underestimates of rock abundance values in these areas. However, the exponential relationship presented in equation (2) may provide clues for estimating the actual mean rock abundance values for those regions with crater densities $>27.5\%$. Furthermore, in other situations when rock detection on images is difficult due to unfavorable illumination conditions, the proposed function can be used to estimate the general rock abundances by referring to the crater densities.

4.3. Relationship Between Rock Abundance and Surface Age

Older surfaces are exposed to more impacts with higher crater density, and as shown in the previous section, higher crater density generally leads to higher rock abundance. It is worth investigating whether there is a correlation between rock abundance and surface age. Based on the previously estimated ages of the five mare units (Im1, Im2, Em1, Em3, and Em4), this study investigates the relationship between mean rock abundance and the surface age of these units, as shown in Figure 10. It should be noted that the other three Rümker plateau units (IR1, IR2, and IR3) are excluded from this analysis due to their different terrain type. Figure 10 shows that in general, older surfaces have larger rock abundance. This can be explained that older surfaces experienced more impacts and consequently featured with more rocky impact craters compared with younger surfaces. Although rocks degrade over time resulting in decreased rock abundances at local scales, the overall rock abundances on older surfaces should be larger than younger surfaces at large scales.
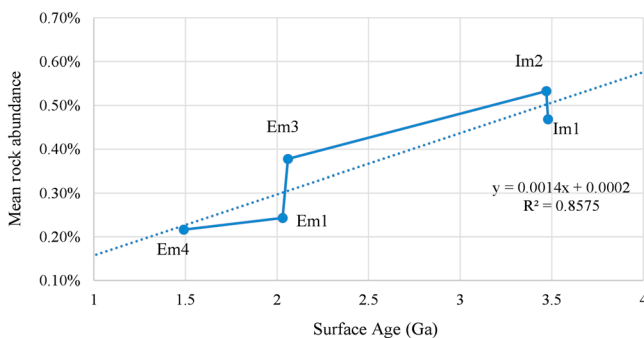
However, for individual craters the situation might be different. Previous studies have noted that young craters are more likely to have elevated rock abundance, as rocks will be degraded over time by space weathering and micrometeorite impacts (Mendell, 1976; Thompson et al., 1974). To verify this finding, this study investigates the rock abundance associated with craters based on the relative ages of craters. The NB model proposed by Charalambous (2014) is used to analyze the relationship between rock abundance and crater maturity. The NB model describes the relationship between the existence probabilities of fragments and the number of

Figure 10. Relationship between rock abundance and surface age.
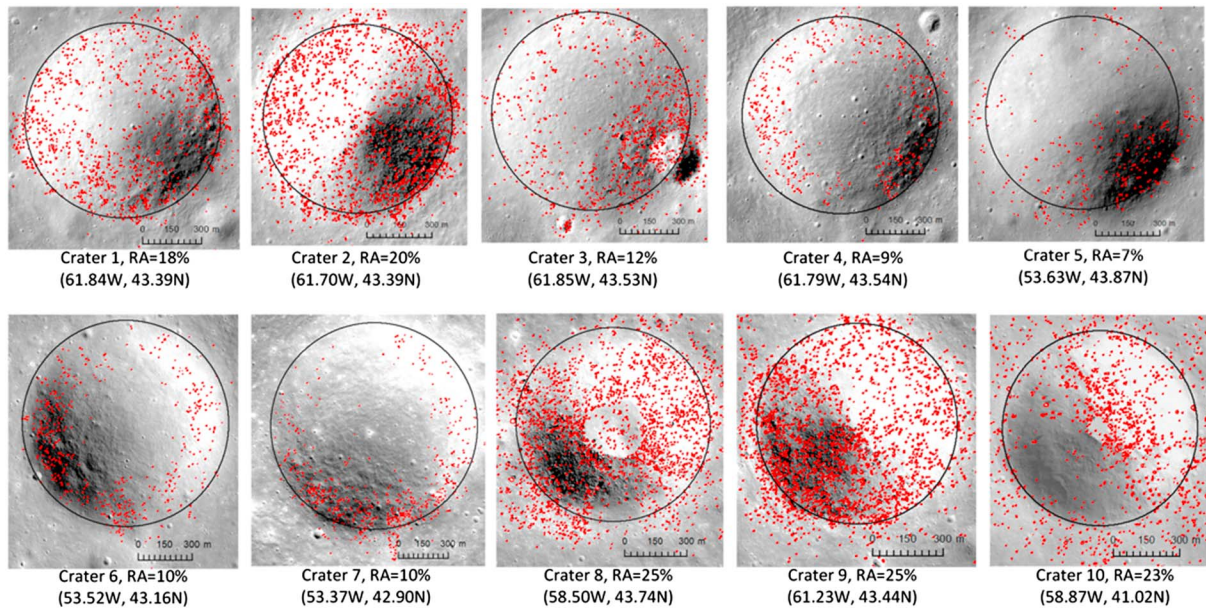
(a) 10 craters with similar size (~ 1 km) and good illumination conditions for rock detection, shown on the LRO NAC image mosaic
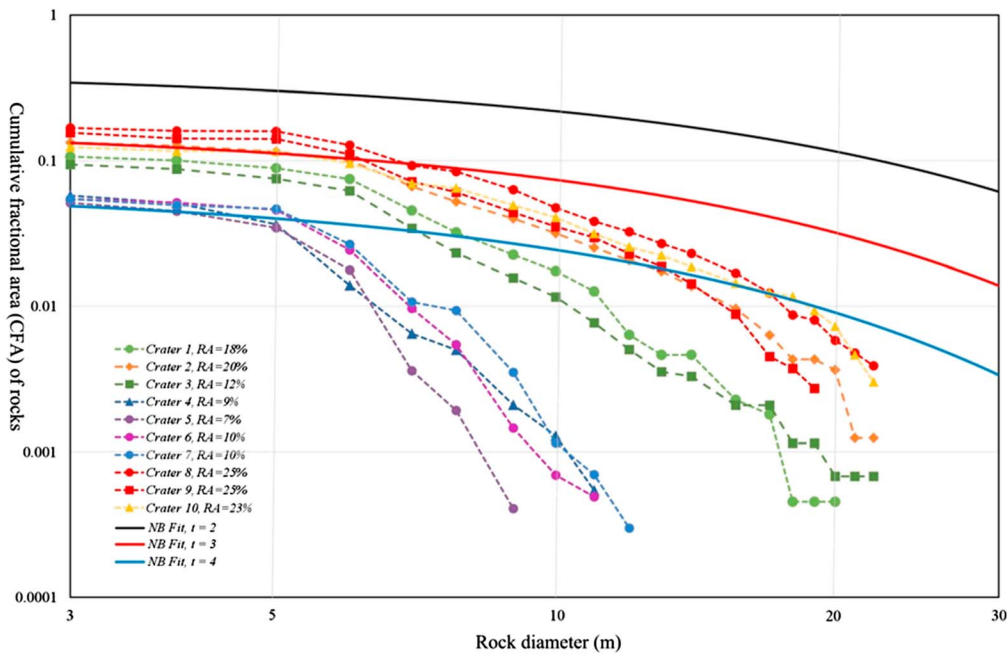
(b) Cumulative fractional area of rocks versus rock diameters and cumulative NB fitting results

Figure 11. Relationship between rock abundance and relative ages of craters. LRO = Lunar Reconnaissance Orbiter; NAC = narrow-angle camera.

fragmentation events. The fracture probability p is only related to the material of the fragments and the existence probabilities of fragments of different sizes can be computed based on p. Mathematically, the NB model presents a trend that the existence probabilities of larger fragments decrease more significantly than smaller ones during the fragmentation events, which is consistent with the previous findings that larger rocks broke down at different rates compared with smaller rocks (Molaro et al., 2015). According to

Charalambous (2014), the fracture probability of particles on the lunar surface is 0.71, and we assume it is the same for the rock materials. Based on this assumption, 10 craters (Crater 1 ~ 10 as shown in Figure 11a) with similar sizes (~ 1 km in diameter) were selected to analyze the relationship between rock abundance and the maturation index t in the NB fragmentation process, as shown in Figure 11b. The rock abundances of these 10 craters range from 7% to 25%. The maturation index t is a parameter in NB model indicating the time of the fragmentation event. A lower t indicates a younger crater age. Given that smaller rocks with large numbers are more appropriate for statistical analysis and crater degradation may refresh the rock populations on the slopes inside crater rims and result in more smaller rocks, emphasis should be placed on the relatively small rocks (e.g., less than 6 m in diameter) shown in Figure 11b. It can be seen in Figure 11b that, for Craters 8 and 9 with the highest rock abundance value of 25%, their CFA curves are higher than the NB fit curve with $t = 3$. For Craters 2 and 10 with rock abundance values of 20% and 23%, their CFA curves are almost overlaid with the $t = 3$ NB fit curve. For Craters 1 and 3 with rock abundances of 18% and 12%, respectively, their corresponding CFA curves are between the NB fit curves with $t = 3$ and $t = 4$. For Craters 4, 5, 6, and 7, their rock abundances are all ≤10%, and their corresponding CFA curves are closer to the NB fit curve with $t = 4$. These results indicate that, in general, there is an inverse correlation between rock abundance and the maturation index t of a crater, which means that for craters with similar size, the higher the rock abundance, the younger the crater is likely to be.

5. Conclusions and Discussion

This paper investigates rock abundance and crater density in the candidate Chang'E-5 landing region. Major findings are as follows:

1. In the candidate landing region, rocks are mostly concentrated around rocky ejecta craters and some are along the wrinkle ridges. About 90% of the region has rock abundance of less than 1%, 9.1% of the region has rock abundance between 1% and 7%, and 0.9% of the region has rock abundance greater than 7%.

2. In the candidate landing region, the average crater density is about 250 craters (≥ 100 m in diameter) per 100 km^2 area, with on average 13.5% of the area covered by craters. The surface ages of the geologic units in the region estimated from crater SFD analysis indicate that the eastern part of the region is younger than the western part, which is generally consistent with previous studies (Hiesinger et al., 2003; Qian et al., 2018).

3. Joint analysis of rock abundance and crater density identifies local areas inside the candidate landing region with relatively high rock abundance or crater density.

4. Joint analysis of rock abundance and crater density also shows an exponential relationship between overall rock abundance and crater density, and a roughly linear relationship between overall rock abundance and surface age. Analysis also indicates an inverse correlation between rock abundance and the relative maturation of craters.

The presented research and results are useful for understanding rock and crater distributions in the candidate landing region of the Chang'E-5 mission and will be helpful for identifying suitable landing sites for the Chang'E-5 lander. Rock abundance, crater density, and their joint analysis results also provide fresh insights into lunar surface geology about the relationships among rock abundance, crater density, maturation of craters, and surface ages.

References

Bandfield, J. L., Ghent, R. R., Vasavada, A. R., Paige, D. A., Lawrence, S. J., & Robinson, M. S. (2011). Lunar surface rock abundance and regolith fines temperatures derived from LRO diviner radiometer data. *Journal of Geophysical Research*, *116*, E00H02. https://doi.org/10.1029/2011JE003866

Barker, M., Mazarico, E., Neumann, G., Zuber, M., Haruyama, J., & Smith, D. (2016). A new lunar digital elevation model from the Lunar Orbiter Laser Altimeter and SELENE terrain camera. *Icarus*, *273*, 346–355. https://doi.org/10.1016/j.icarus.2015.07.039

Bart, G., & Melosh, H. (2010a). Impact into lunar regolith inhibits high-velocity ejection of large blocks. *Journal of Geophysical Research*, *115*, E08004. https://doi.org/10.1029/2009JE003441

Bart, G., & Melosh, H. (2010b). Distribution of boulders ejected from lunar craters. *Icarus*, *209*(2), 337–357. https://doi.org/10.1016/j.icarus.2010.05.023

Basilevsky, A., Abdrakhimov, A., Head, J., Pieters, C., Wu, Y., & Xiao, L. (2015). Geologic characteristics of the Luna 17/Lunokhod 1 and Chang'E-3/Yutu landing sites, northwest Mare Imbrium of the Moon. *Planetary and Space Science*, *117*, 385–400. https://doi.org/10.1016/j.pss.2015.08.006

Basilevsky, A., Head, J., & Horz, F. (2013). Survival times of meter-sized boulders on the surface of the Moon. *Planetary and Space Science*, *89*, 118–126. https://doi.org/10.1016/j.pss.2013.07.011

Brady, T., Robertson, E., Epp, C., Paschall, S., & Zimpfer, D. (2009). Hazard detection methods for lunar landing. In *Aerospace conference, 2009 IEEE* (pp. 1–8). Big Sky, MT.

Charalambous, C. (2014). On the evolution of particle fragmentation with applications to planetary surfaces. PhD thesis, Imperial College London, London, United Kingdom.

Christensen, P. R. (1986). The spatial distribution of rocks on Mars. *Icarus*, *68*(2), 217–238. https://doi.org/10.1016/0019-1035(86)90020-5

Cintala, M. J., & McBride, K. M. (1995). Block distribution on the lunar surface: A comparison between measurements obtained from surface and orbital photography, NASA Technical Report, NASA-TM-104804, NAS 1.15:104804, S-782, NIPS-96-07702, 46 p.

Di, K., Xu, B., Peng, M., Yue, Z., Liu, Z., Wan, W., & Zhou, J. (2016). Rock size-frequency distribution analysis at the Chang'E-3 landing site. *Planetary and Space Science*, *120*, 103–112. https://doi.org/10.1016/j.pss.2015.11.012

Ghent, R. R., Hayne, P. O., Bandfield, J. L., Campbell, B. A., Allen, C. C., Carter, L. M., & Paige, D. A. (2014). Constraints on the recent rate of lunar ejecta breakdown and implications for crater ages. *Geology*, *42*(12), 1059–1062. https://doi.org/10.1130/G35926.1

Gilvarry, J. (1961). Fracture of brittle solids. I. Distribution function for fragment size in single fracture (theoretical). *Journal of Applied Physics*, *32*(3), 391–399. https://doi.org/10.1063/1.1736016

Golombek, M., Grant, J., Kipp, D., Vasavada, A., Kirk, R., Fergason, R., et al. (2012). Selection of the Mars Science Laboratory landing site. *Space Science Reviews*, *170*(1–4), 641–737. https://doi.org/10.1007/s11214-012-9916-y

Golombek, M., Kipp, D., Warner, N., Daubar, I. J., Fergason, R., Kirk, R. L., & Campbell, B. A. (2017). Selection of the InSight landing site. *Space Science Reviews*, *211*(1–4), 5–95. https://doi.org/10.1007/s11214-016-0321-9

Golombek, M., & Rapp, D. (1997). Size-frequency distributions of rocks on Mars and Earth analog sites: Implications for future landed missions. *Journal of Geophysical Research*, *102*(E2), 4117–4129. https://doi.org/10.1029/96JE03319

Golombek, M. P., Haldemann, A., Forsberg-Taylor, N., Di Maggio, E., Mellon, M., & Matijevic, J. (2003). Rock size-frequency distributions on Mars and implications for Mars Exploration Rover landing safety and operations. *Journal of Geophysical Research*, *108*(E12), 8086. https://doi.org/10.1029/2002JE002035

Guo, D., Liu, J., Head, J. W. III, & Kreslavsky, M. A. (2018). Lunar Orientale impact basin secondary craters: Spatial distribution, size-frequency distribution and estimation of fragment size. *Journal of Geophysical Research: Planets*, *123*, 1344–1367. https://doi.org/10.1029/2017JE005446

Hartmann, W. K. (1964). On the distribution of lunar crater diameters. *Communications of the Lunar and Planetary The Laboratory*, *2*, 197–204.

Hiesinger, H., Head, J. W., Wolf, U., Jaumann, R., & Neukum, G. (2003). Ages and stratigraphy of mare basalts in Oceanus Procellarum, Mare Nubium, Mare Cognitum, and Mare Insularum. *Journal of Geophysical Research*, *108*(E7), 5056. https://doi.org/10.1029/2002JE001985

Huertas, A., Cheng, Y., & Madison, R. (2006). Passive imaging based multi-cue hazard detection spacecraft safe landing. IEEE Aerospace Conference, Big Sky, Montana, March 4–11.

Krishna, N., & Kumar, P. S. (2016). Impact spallation process on the Moon: A case study from the size and shape analysis of ejecta boulders and secondary craters of Censorinus crater. *Icarus*, *264*, 274–299. https://doi.org/10.1016/j.icarus.2015.09.033

Li, C., Liu, J., Ren, X., Zuo, W., Tan, X., Wen, W., et al. (2015). The Chang'e 3 mission overview. *Space Science Reviews*, *190*(1–4), 85–101. https://doi.org/10.1007/s11214-014-0134-7

Li, Y., & Wu, B. (2018). Analysis of rock abundance on lunar surface from orbital and descent images using automatic rock detection. *Journal of Geophysical Research: Planets*, *123*, 1061–1088. https://doi.org/10.1029/2017JE005496

Mendell, W. (1976). Degradation of large, period II lunar craters. Paper presented at the Lunar and Planetary Science Conference.

Molaro, J. L., Byrne, S., & Langer, S. A. (2015). Grain-scale thermoelastic stresses and spatiotemporal temperature gradients on airless bodies, implications for rock breakdown. *Journal of Geophysical Research: Planets*, *120*, 255–277. https://doi.org/10.1002/2014JE004729

Moore, H., Hutton, R., Clow, G., & Spitzer, C. (1987). Physical properties of the surface materials at the Viking landing sites on Mars (2330–7102), Retrieved from https://pubs.er.usgs.gov/publication/pp1389, 222 p.

Moore, H., & Keller, J. (1991). Surface-material maps of Viking landing sites on Mars. Lunar and Planetary Science Conference (Vol. 21, 807 pp.). Houston, TX.

Neukum, G. (1983). *Meteoriten bombardement and datierung planetarer oberfluchen* (p. 186). Habilitation Dissertation for Faculty Membership, University of Munich, Munich, Germany.

Neukum, G., Ivanov, B. A., & Hartmann, W. K. (2001). Cratering records in the inner solar system in relation to the lunar reference system. *Space Science Reviews*, *96*(1/4), 55–86. https://doi.org/10.1023/A:1011989004263

Nowicki, S., & Christensen, P. (2007). Rock abundance on Mars from the thermal emission spectrometer. *Journal of Geophysical Research*, *112*, E05007. https://doi.org/10.1029/2006JE002798

Ouyang, Z. Y., Li, C., Zou, Y., Zhang, H., Lv, C., Liu, J., et al. (2010). Preliminary scientific results of Chang'E-1 lunar orbiter. *Science China*, *53*(11), 1565–1581. https://doi.org/10.1007/s11430-010-4056-2

Pajola, M., Rossato, S., Baratti, E., Pozzobon, R., Quantin, C., Carter, J., & Thollot, P. (2017). Boulder abundances and size-frequency distributions on Oxia Planum-Mars: Scientific implications for the 2020 ESA ExoMars rover. *Icarus*, *296*, 73–90. https://doi.org/10.1016/j.icarus.2017.05.011

Qian, Y. Q., Xiao, L., Zhao, S. Y., Zhao, J. N., Huang, J., Flahaut, J., & Wang, G. X. (2018). Geology and scientific significance of the Rümker region in northern Oceanus Procellarum: China's Chang'E-5 landing region. *Journal of Geophysical Research: Planets*, *13*, 1407–1430. https://doi.org/10.1029/2018JE005595

Robbins, S. J., & Hynek, B. M. (2014). The secondary crater population of Mars. *Earth and Planetary Science Letters*, *400*, 66–76. https://doi.org/10.1016/j.epsl.2014.05.005

Robinson, M. S., Brylow, S. M., Tschimmel, M., Humm, D., Lawrence, S. J., Thomas, P. C., et al. (2010). Lunar reconnaissance orbiter camera (LROC) instrument overview. *Space Science Reviews*, *150*(1-4), 81–124. https://doi.org/10.1007/s11214-010-9634-2

Rosa, D., Bussey, B., Cahill, J. T., Lutz, T., Crawford, I. A., Hackwill, T., et al. (2012). Characterisation of potential landing sites for the European Space Agency's lunar Lander project. *Planetary and Space Science*, *74*(1), 224–246. https://doi.org/10.1016/j.pss.2012.08.002

Scott, D. H., & Eggleton, R. E. (1973). Geologic map of the Rümker quadrangle of the Moon. Flagstaff: USGS Astrogeology Science Center. No. 805.

Serrano, N., & Seraji, H. (2007). Landing site selection using fuzzy rule-based reasoning. In *Robotics and automation, 2007 IEEE International Conference*, Roma, Italy (pp. 4899–4904).

Shoemaker, E. M., Batson, R. M., Bean, A. L., Conrad, C. Jr., Dahlem, D. H., Goddard, E. N., et al. (1970). *Preliminary geologic investigation of the Apollo 12 landing site: Part A: Geology of the Apollo 12 Landing Site* (p. 44). Washington, DC: National Aeronautics and Space Administration.

Shoemaker, E. M., Batson, R. M., Holt, H. E., Morris, E. C., Rennilson, J. J., & Whitaker, E. A. (1968). Television observations from Surveyor 3. *Journal of Geophysical Research*, *73*(12), 3989–4043. https://doi.org/10.1029/JB073i012p03989

Thompson, T., Masursky, H., Shorthill, R., Tyler, G., & Zisk, S. (1974). A comparison of infrared, radar, and geologic mapping of lunar craters. *The Moon*, *10*(1), 87–117. https://doi.org/10.1007/BF00562019

Wang, Y., Zhu, X., & Wu, B. (2018). Automatic Detection of Individual oil palm trees from UAV images using HOG features and an SVM classifier. *International Journal of Remote Sensing*. https://doi.org/10.1080/01431161.2018.1513669

Watkins, R. N., Jolliff, B. F., Fogerty, C., Mistick, K., Singer, K. N., & Lawrence, S. J. (2018). Boulder distribution around young, Small lunar impact craters. In 49th Lunar and Planetary Science Conference, The Woodlands, TX, 2018, Abstract 1201.

Watkins, R. N., Mistick, K., Jolliff, B. L., & Lawrences, S. J. (2018). Boulder distribution around young lunar impact craters: Case study of south ray crater. In 49th Lunar and Planetary Science Conference, The Woodlands, TX, 2018, Abstract 1146.

Wilhelms, D. E., John, F., & Trask, N. J. (1987). *The geologic history of the Moon* (p. 302). Denver, CO: USGS.

Wu, B., Li, F., Ye, L., Qiao, S., Huang, J., Wu, X., & Zhang, H. (2014). Topographic modeling and analysis of the landing site of Chang'E-3 on the Moon. *Earth and Planetary Science Letters*, *405*, 257–273. https://doi.org/10.1016/j.epsl.2014.09.009

Xiao, Z., & Strom, R. G. (2012). Problems determining relative and absolute ages using the small crater population. *Icarus*, *220*(1), 254–267. https://doi.org/10.1016/j.icarus.2012.05.012

Zeng, X., Zuo, W., Zhang, Z., Liu, Y., & Li, C. (2017). Topographic and geologic analysis of the pre-Selection landing sites for Chang'E-5 (CE-5) lunar sample returning mission of China. Paper presented at 19th EGU General Assembly, EGU, Vienna, Austria.

Zou, Y. L., & Li, W. (2017). Scientific visions of lunar research-station from China. Paper presented at 48th Lunar and Planetary Science Conference, Lunar and Planetary Institute, The Woodlands.